International Journal of GEOMATE, Feb., 2024 Vol.26, Issue 114, pp.50-59
ISSN: 2186-2982 (P), 2186-2990 (O), Japan, DOI: https://doi.org/10.21660/2024.114.4192
Geotechnique, Construction Materials and Environment

ASSESSMENT OF LIQUEFACTION RISK WITH UNIDENTIFIED SEISMIC PARAMETERS FOR NEWLY-DISCOVERED FAULTS: NUMERICAL ANALYSIS

Kusmanto[1], *Sito Ismanti[2] and Angga Fajar Setiawan[3]

[1,2,3] Department of Civil and Environmental Engineering, Universitas Gadjah Mada, Indonesia

*Corresponding Author, Received: 17 Oct. 2023, Revised: 28 Dec. 2023, Accepted: 29 Dec. 2023

ABSTRACT: Earthquakes can trigger liquefaction, which can cause soil to lose its strength and stability. Ambon City is vulnerable to large earthquakes owing to tectonic movements. Therefore, accurate analyses are required to assess the seismic hazards and liquefaction potential. This study aims to determine the hazard spectrum and artificial earthquakes to estimate liquefaction potential through numerical analysis. This study conducts a comprehensive analysis to accurately investigate liquefaction potential using deterministic seismic analysis based on new faults and nonlinear analysis with a two-dimensional finite element approach. The results of this study show that nonlinear analysis can effectively account for the increase in pore water pressure (PWP) during earthquake shaking, thus providing more detailed information on the changes in effective stress and PWP in different soil layers. The effective stress did not decrease in the unsaturated soil layers. However, in the saturated soil layers, the effective stress decreased as PWP increased during the shaking period. Liquefaction potential was predicted before the earthquake in soils with N-SPT <15 and continued to increase in all soil layers until the end of the shaking period. This study also showed the behavior of soils that experienced significant amplification. The peak ground acceleration in the bedrock increased from 0.408 to 0.952 g at the surface. The amplification factor is 2.33, indicating that the soil at the site is susceptible to high-amplitude earthquakes. The results of this study indicate that areas near faults are vulnerable to seismic hazards and susceptible to liquefaction in all the soil layers. The results indicated the need to implement effective and efficient mitigation strategies for infrastructure planning and development in these areas.

Keywords: Pore water pressure, Liquefaction, Effective stress, Earthquake, Fault

1. INTRODUCTION

Earthquakes can damage buildings and threaten human lives. One of the effects of earthquakes is liquefaction [1], in which saturated sandy soils can become liquid because of increased pore water pressure (PWP) caused by strong shaking. This increase can also reduce the strength and stiffness of the soil, causing it to lose its bearing capacity [2].

Tectonic activity, such as plate movement along active faults, can trigger earthquakes [3]. The eastern part of Indonesia, including Ambon City, is known to have a high level of tectonic activity [4]. Ambon City often experiences significant earthquakes because of its complex tectonic conditions. The September 2019 earthquake in Ambon City caused many casualties and extensive building damage, suggesting the possibility of unidentified potential faults [5]. A recent study found several northeast-trending fault lines in Ambon City [6]. However, incomplete identification of these fault parameters makes seismic hazard analysis and liquefaction potential assessment difficult.

Previously, Sengara and Sulaiman [7] used a 2D Finite Difference Method (FDM) with an efficient stress model to assess the impact of relative soil density on the likelihood of liquefaction. In contrast, a 2D Finite Element Method (FEM) with a linear-elastic model was used to investigate the liquefaction potential [8]. Furthermore, an equivalent linear model was used to investigate the response of concrete caisson walls in liquefaction-prone soils [9].

However, the linear and equivalent linear models have certain limitations. The excess PWP can only be determined at the end of the shaking period and not during the earthquake shaking. Therefore, the effective stress could not be modified during shaking. Consequently, excess PWP can be calculated based only on the peak dynamic shear stress.

In contrast, this study uses a numerical 2D nonlinear finite element method to capture the behavior of excess PWP during earthquake shaking. This allows for a more accurate assessment of the liquefaction potential that matches field conditions. Consistent with this, nonlinear analyses can produce more accurate soil response predictions than linear or equivalent linear analyses [10]. This study aims to assess the seismic hazards and liquefaction potential in Ambon City, Indonesia, which is prone to earthquakes due to tectonic movements. This study can provide additional information for predicting seismic hazards from faults in which some parameters are not identified.

2. RESEARCH SIGNIFICANCE

This study is highly significant for determining the impacts of earthquakes and soil liquefaction phenomena in specific areas. Using the numerical 2D nonlinear finite element method, this study can capture the behavior of excess PWP during shaking, enabling a more accurate assessment to predict liquefaction potential. In addition, this study provides insights into seismic hazard analysis of faults for which some parameters are unknown. Thus, the results of this study can provide useful information for researchers and practitioners managing earthquake and soil liquefaction risk.

3. METHODOLOGY

3.1 Study Area

This study was conducted in the coastal area of Ambon City, the capital city of the Maluku Province, Indonesia. The region has unique geographical features with major geological formations consisting of alluvial surface deposits, including gravel, small stones, sand, clay, and plant remains [11]. The soil investigation was conducted by drilling six boreholes using the Standard Penetration Test (SPT) method, the soil stratigraphy of which is shown in Fig. 1. However, the sampling was limited to site BH-01 at a certain depth. The results of detailed soil property investigations are presented in Table 2.

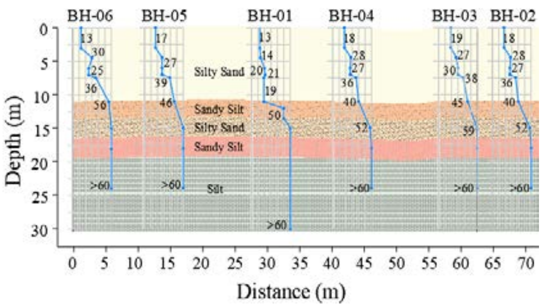

Fig.1 Soil stratigraphy identified through laboratory test results at the site

3.2 Estimation of Unknown Fault Parameters

A study by [6] identified a new fault close to Ambon City that extends 34 km from Ambon Bay to the Liang coastline (Fig. 2). This new fault may have caused an earthquake of M_w 6.9 earthquake. However, the parameters required to calculate the potential seismic hazard of this fault were incomplete. Therefore, this study estimated the seismic hazard potential of a new fault using a deterministic method based on [12]. This deterministic method suits individual earthquake sources such as faults and is particularly effective for assessing seismic hazards in specific geological settings [13].

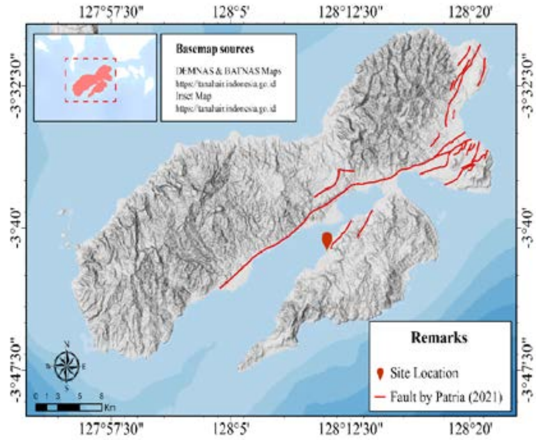

Fig.2 The location of the Ambon fault modified from [6]

3.2.1 Dip Angle (δ)

A study by [6] indicated that the fault in Ambon can be classified as normal. This result makes it possible to determine the dip angle (δ) following the recommendation of [14], which states that the dip angle (δ) for normal faults is 50°. The direction of the dip angle (δ) and fault orientation are shown in Fig. 3.

3.2.2 Fault Width (W)

This study used the Wells and Coppersmith equation [15] to determine fault width. This equation was used because it is a reasonable empirical method widely used in seismological research [12]. Using Eq. (1) and magnitude (M) of 6.9, the value of W was 18.84 km.

$$W = 10^{-1.14+0.35\,M} \tag{1}$$

3.2.3 Depth to Top of Rupture (Z_{TOR})

The approach developed in [12] was adopted to determine the Z_{TOR}. This approach considers hypo central depth (Z_{HYP}), dip angle (δ), and fault width (W). Furthermore, the assumption from [16] was used, which states that the hypocenter is approximately 60% below the fault width. Using Eq. (2) and moment magnitude (M) of 6, the hypocentral depth (Z_{HYP}) was obtained by 11.29 km. Furthermore, the value of Z_{TOR} was calculated using Eq. (3), with values of W = 18.84 km and δ = 50° and a Z_{TOR} of 2.63 km was obtained.

$$Z_{HYP} = 11.24 - 0.2M \tag{2}$$

$$Z_{TOR} = max\,[(Z_{HYP} - 0.6\,W\,sin\,\delta), 0] \tag{3}$$

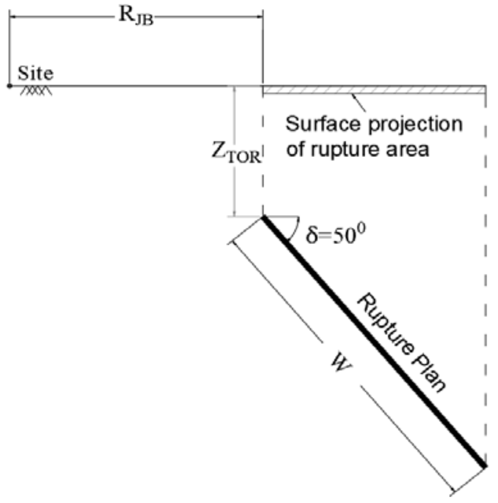

Fig.3 Measurement of Dip Angle (Modified from [12])

3.2.4 Strike-Perpendicular Distance to Rupture (R_x)

The Joyner-Boore Distance (R_{JB}) and azimuth (α) values were used to determine the perpendicular distance from the location to the fault rupture plane (R_x). ArcGIS Pro software was used to determine R_{JB} and α values, and the results are shown in Fig. 4. The determination of α was based on the provisions shown in Fig. 5. Furthermore, based on Fig. 6, the research location was categorized as Case 7, whose equation is shown in Eq. (4).

$$R_x = R_{JB} \; Sin\, \alpha \tag{4}$$

In this case, R_{JB} was determined to be 0.58 km with an α value of -141˚. Furthermore, R_x can be calculated using Eq. (4), as suggested in [12], resulting in an R_x value of 0.37 km.

3.2.5 Rupture-to-Site Distance (R_{RUP})

To determine the R_{RUP}, Eq. (5), as proposed by [12], was used for $\delta \neq 90$. R_{RUP}' is the closest distance to the fault plane from the location parallel to the fault plane of the area in a given direction. In contrast, R_y is the closest distance from the location to the rupture area and is measured parallel to the strike. Eq. (6) was used to determine the R_{RUP} value because $R_x < Z_{TOR} \tan \delta$. To calculate R_y, Eq. (7) was used because α is outside of 0°, ±90°, and ±180°. Based on this calculation, R_{RUP}' was obtained as 2.66 km and R_y as 0.45 km. The resulting R_{RUP} was 2.69 km.

$$R_{RUP} = \sqrt{(R_{RUP}')^2 + R_Y{}^2} \tag{5}$$

$$R_{RUP}' = \sqrt{R_x{}^2 + Z_{TOR}{}^2} \tag{6}$$

$$R_y = |R_x \cot \alpha| \tag{7}$$

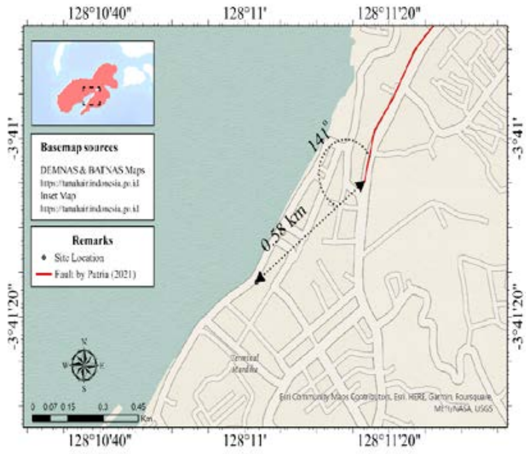

Fig.4 Measurement of R_{JB} modified from [6]

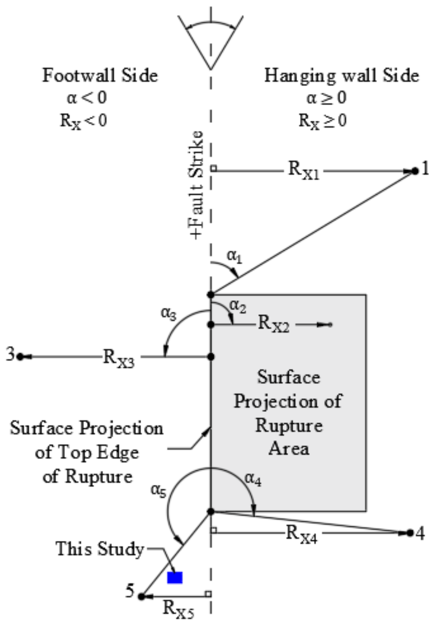

Fig.5 Mechanism of azimuth determination [12]

3.3 Determination of the Response Spectrum

The Next Generation Attenuation (NGA) West 2 model was used to develop response spectra. The input parameters are listed in Table 1. The NGA West 2 model has been validated to provide accurate and consistent predictions, and has a relatively narrow deviation range [17,18]. Next, an attenuation equation with an equal weight of 1 was selected. The selected attenuation equations are Abrahamson Silva and Kamai [19], Boore Stewart Seyhan and Atkinson [20], Campbell and Bozorgina [21], and Chiou and Youngs [22]. The NGA West 2 model produces a target response spectrum, as shown in Fig. 7. The obtained response spectrum was larger than that obtained using the probabilistic method from the Indonesian Earthquake Code [23]. The response spectrum serves as the target spectrum for the development of artificial earthquakes.

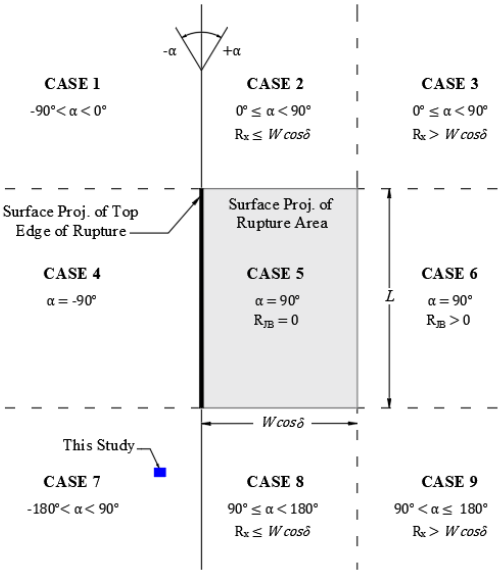

Fig.6 Case type in determining R_y [12]

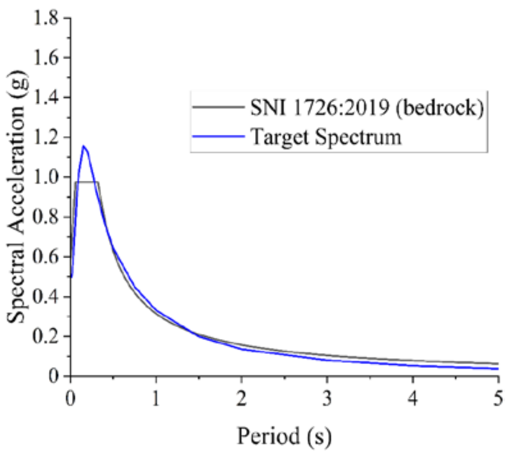

Fig.7 Target response spectrum modified from NGA Model 2

3.4 Developing Artificial Earthquake

This study used the SeisMoartif software with an academic license to develop an artificial earthquake model. The model used was the Synthetic Accelerogram Generation & Adjustment method developed in [24]. Using simplified earthquake parameters, the model generated a more realistic artificial earthquake. The earthquake parameters were M_w 6.9, based on [6], and a hypocentral distance of approximately 10 km, as recommended by the user manual. The Regime type used was a regime of active tectonic extension with a near-field option.

Table 1 Input parameters in the NGA West 2 model

Parameters	Units	Input
Damping ratio	%	5
Region	-	Global
Fault Type	-	Normal
Magnitude	M_w	6.9
R_{RUP}	km	2.69
R_x	km	0.37
R_{JB}	km	0.58
Z_{TOR}	km	2.63
Width	km	18.84
Dip	degree	50
Vs_{30}	m/s	760
$Z_{1.0}$	km	(ask14:0.05, cy14:0.04)
$Z_{2.5}$	km	0.6068
Z_{hyp}	km	11.29
Epsilon	-	0
GMM Average	-	Geometric

Furthermore, the ENA NEHRP B-C Boundary model with a shear wave velocity (Vs_{30}) of approximately 760 m/s was selected to consider the site effect and obtain an artificial earthquake at the bedrock level. The artificial earthquake, shown in Fig. 8, was obtained by adjusting the premade target spectrum. The artificial earthquake had a peak ground acceleration (PGA) of 0.408 g and a duration length of 14.82 s.

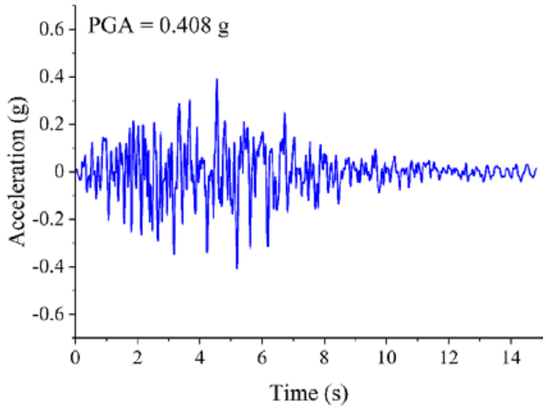

Fig.8 The artificial earthquake generated using Seismoartif

3.5 2D Finite Element Method Modeling

3.5.1 Soil Parameters

The QUAKE/W tool of GeoStudio Software was used to perform the nonlinear numerical analysis. This analysis modeled the soil cross-section with a mesh area of 0.5 x 0.5 m (Fig. 9). The parameters used in the material input for QUAKE/W are as follows:

– The unit weight of the soil (ρ) was determined by referring to borehole data presented in Table 2.

- The soil density was determined based on the correlation of the N-SPT from the borehole, according to [25,26].
- Cohesion (c) was determined based on [27] in Eq. (8).

$$c = -16.5 + 2.15\,N \quad \text{For } N \geq 10 \text{ to } 30 \qquad (8)$$

Where c is the cohesion in kPa, and N is the value of the SPT.

- The friction angle (φ) of the intermediate soil was determined using [27] in Eqs. (9-10).

$$\varphi = 7N \quad \text{For } N \leq 4 \qquad (9)$$

$$\varphi = 27.12 + 0.2857N \quad \text{For } N > 4 \text{ to } 50 \qquad (10)$$

Where φ represents the friction angle (in degrees), and N is the value of the SPT.

- The damping ratio (D) was initially assumed as 5% or 0.05, and the maximum damping ratio (D_{max}) was 0.10.
- Poisson's ratio (υ) for granular soil was determined based on [27] in Eqs. (11-12).

$$\upsilon = 0.2 + 0.01\,N \quad \text{For } N \geq 0 \text{ to } 20 \qquad (11)$$

$$\upsilon = 0.2 + 0.005\,N \quad \text{For } N \geq 20 \text{ to } 50 \qquad (12)$$

Where υ is Poisson's ratio, and N is the value of the SPT.

3.5.2 Shear Modulus Function

In this study, the determination of the shear modulus (G_{max}) relied on a sophisticated software function coupled with a cohesive soil-estimation method. This approach was imperative because of the heterogeneous nature of the soil at the site, which comprised a blend of sand and silt. The calculation of G_{max} using these functions necessitates the utilization of specific input parameters, which are detailed as follows:

- The overconsolidation ratio (OCR) was assumed to be normally consolidated or 1.00, based on [28].
- The Plasticity Index (PI) was determined by referring to the laboratory data in Table 2.
- The void ratio (e) is determined based on [29] in Eq. (13).

$$e = 1.202N^{-0.217} \qquad (13)$$

Where e is the void ratio, and N is the SPT value.

- The coefficient of the earth pressure at rest (K_0), as recommended by [26], can be calculated using Eq. (14).

$$K_0 = 1 - \sin\emptyset \qquad (14)$$

Where (K_0) is the coefficient of earth pressure at rest and $\emptyset$ is the friction angle.

Table 2 Input materials in QUAKE/W

Depth (m)	N	ρ (kN/m^3)	Soil type	Density	υ	c (kPa)	Φ (°)	K_0	PI (%)	e
1.00	13	17.10	Silty Sand	Medium Dense	0.33	11.45	30.83	0.49	2.080	0.69
2.20	13	17.10	Silty Sand	Medium Dense	0.33	11.45	30.83	0.49	2.080	0.69
3.00	13	19.46	Silty Sand	Medium Dense	0.33	11.45	30.83	0.49	2.080	0.69
4.45	14	19.46	Silty Sand	Medium Dense	0.34	13.60	31.12	0.48	2.080	0.68
6.00	20	19.46	Silty Sand	Medium Dense	0.30	26.50	32.83	0.46	2.080	0.63
7.00	21	19.46	Silty Sand	Medium Dense	0.31	28.65	33.12	0.45	2.080	0.62
7.45	19	19.46	Silty Sand	Medium Dense	0.39	24.35	32.55	0.46	2.080	0.63
8.00	19	19.46	Silty Sand	Medium Dense	0.39	24.35	32.55	0.46	2.080	0.63
9.50	19	19.46	Silty Sand	Medium Dense	0.39	24.35	32.55	0.46	2.080	0.63
11.00	19	19.46	Silty Sand	Medium Dense	0.39	24.35	32.55	0.46	2.080	0.63
12.00	50	18.94	Sandy Silt	Very Dense	0.45	91.00	41.41	0.34	1.610	0.51
13.50	50	18.94	Sandy Silt	Very Dense	0.45	91.00	41.41	0.34	1.610	0.51
15.00	60	19.52	Silty Sand	Very Dense	0.45	112.50	44.26	0.30	0.280	0.49
16.50	60	19.52	Silty Sand	Very Dense	0.45	112.50	44.26	0.30	0.280	0.49
18.00	60	21.02	Sandy Silt	Very Dense	0.45	112.50	44.26	0.30	1.230	0.49
19.50	60	21.02	Sandy Silt	Very Dense	0.45	112.50	44.26	0.30	1.230	0.49
21.00	60	21.02	Silt	Very Dense	0.45	112.50	44.26	0.30	1.870	0.49
22.50	60	21.02	Silt	Very Dense	0.45	112.50	44.26	0.30	1.870	0.49
24.00	60	21.02	Silt	Very Dense	0.45	112.50	44.26	0.30	1.870	0.49
27.00	60	21.02	Silt	Very Dense	0.45	112.50	44.26	0.30	1.870	0.49
30.00	60	21.02	Silt	Very Dense	0.45	112.50	44.26	0.30	1.870	0.49

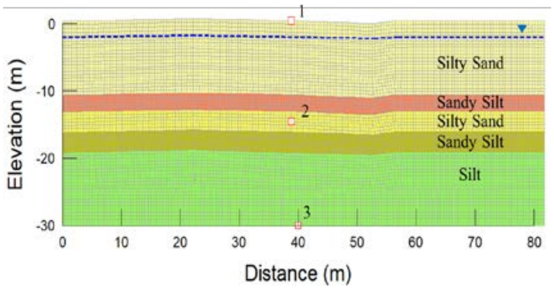

Fig.9 Soil modeling in QUAKE/W

3.5.3 MFS pore-pressure Functions

In this study, the *PWP* model was developed by [30] and recommended by the QUAKE/W user manual. This model assumes an undrained loading condition that influences the volumetric strain owing to the stress increase in the drained condition. The model also assumes that water is incompressible and that the volume does not change during loading. It did not undergo any volume changes during the loading. Therefore, the change in the pore pressure is directly related to the volume change in the soil or material.

3.5.4 Recoverable Modulus Functions

In the analysis of the changes in pore pressure, there is a correlation with the recoverable modulus, also known as the rebound modulus. This condition refers to the ability of a material to recover part or all of its elastic modulus after temporary deformation, such as that occurring during an earthquake. Temporary deformation, such as that occurring during an earthquake, is used in the analysis and can be determined using the function features in QUAKE/W software.

3.5.5 Steady-State Strength

This study adopted the concepts of collapsed surface and steady-state strength supported by QUAKE/W. This concept assumes that sandy soil can have a grain structure that can collapse, causing a decrease in the shear strength under undrained conditions. The two parameters included in the analysis were steady-state strength (C_{ss}) and collapse surface angle (ϕ_L). Based on the recommendations of [31,32], a C_{ss} value of 2 kPa and ϕ_L value of 18.5 were used.

3.6 Boundary Conditions

During the initial and dynamic analyses, separate boundary conditions were used in the x- and y-directions. Initially, the *x*-boundary condition was used for the side layer, indicating no horizontal deformation, and the *x-y* boundary condition was used for the bottom layer, indicating no horizontal or vertical deformation. However, the *y*-boundary condition for the side layers in the dynamic analysis indicated no vertical deformation. In contrast, the *x-y* boundary condition of the bottom layer remained the same. This approach allows the modeling of soil behavior under actual earthquake-shaking conditions.

4. RESULTS AND DISCUSSION

4.1 Effective Stress

The analysis using QUAKE/W software in this study showed a significant decrease in effective stress, as shown in Figs. 10–11. The results indicate that the effective stress in the unsaturated soil layer was relatively constant during shaking. However, the water-saturated soil layer experienced a continuous decrease in effective stress, as shown in Fig. 12. The largest decrease in effective stress occurred in the lowest soil layer. This indicates a decrease in the strength and stiffness of water-saturated soil during shaking, which can significantly affect the bearing capacity and stability of the soil.

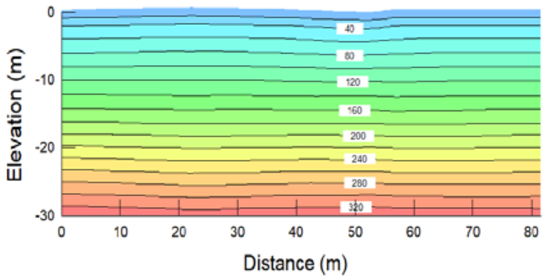

Fig.10 Vertical effective stress during initial shaking periods

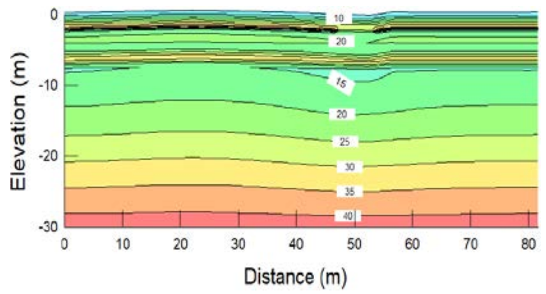

Fig.11 Vertical effective stress during final shaking periods

4.2 Excess Pore Water Pressure

In this study, the analysis showed a significant increase in the excess PWP during shaking, as illustrated in Fig. 13. Excess PWP was not observed on the surface. This condition remains constant until the end of the shock period. However, the excess PWP increased significantly in the middle and lower soil layers. The results also show that, as the soil deepens, the value of excess PWP also increases. Nonlinear analysis successfully explained the increase in PWP during the shock period, enabling more accurate modeling and understanding of the changes in PWP in the soil during shaking. This study provides comprehensive information on the PWP changes in different soil layers during earthquakes.

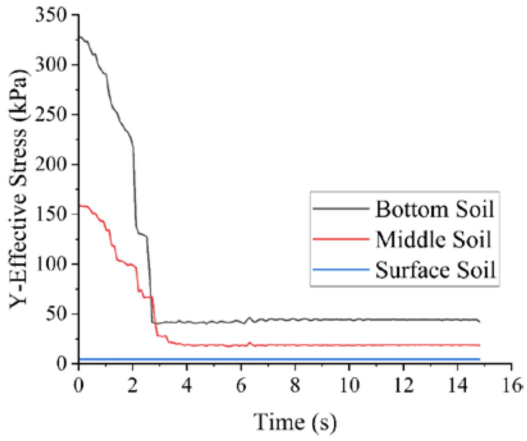

Fig.12 Comparison of vertical effective stress at various shaking periods

4.3 Liquefaction Potential

The liquefaction potential can be measured directly using the features provided by the QUAKE/W analysis. The features are highlighted in yellow. Fig. 14 shows that the liquefaction potential can occur before dynamic analysis, particularly in soils with N-SPT < 15 at depths of 2.2–5 m. Preliminary static analysis was shown to affect the assessment of the liquefaction potential.

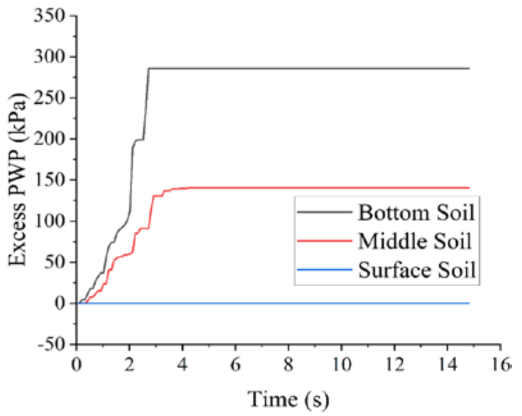

Fig.13 Comparison of excess *PWP* at various shaking periods

The results of this study also show that the liquefaction potential increased significantly in all soil layers starting from a period of 2.02 s, as shown in Fig. 15. At the end of the shaking period, almost all the soils exhibited liquefaction potential, as shown in Fig. 16. This indicates that even moderately dense soils around the coast can experience liquefaction when a strong earthquake occurs.

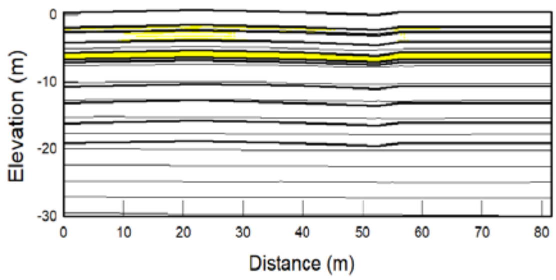

Fig.14 Liquefaction potential during the initial shaking periods

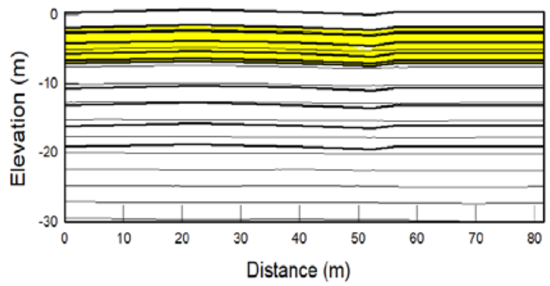

Fig.15 Liquefaction potential during the early shaking periods of 2.02 s

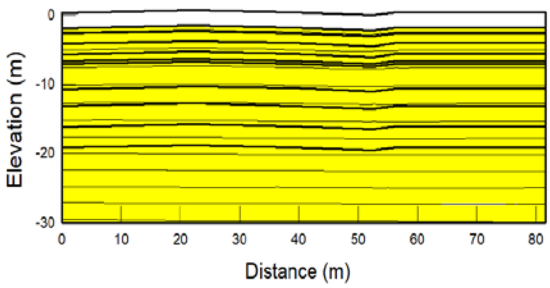

Fig.16 Vertical effective stress at the end of the shaking periods

4.4 Ground Response during Earthquakes

The results of the soil response analyses indicate the presence of amplification phenomena at the site. There was a significant increase in PGA from the bedrock to the ground surface, from 0.408 to 0.952 g (Fig. 17). The amplification factors were determined to be 2.33. This study also demonstrated a significant increase in the response spectrum. Fig. 18 shows that the spectral acceleration at the surface exceeded the spectral acceleration for site class E

[23] for periods before 1.00 s. However, the spectral acceleration decreased significantly.

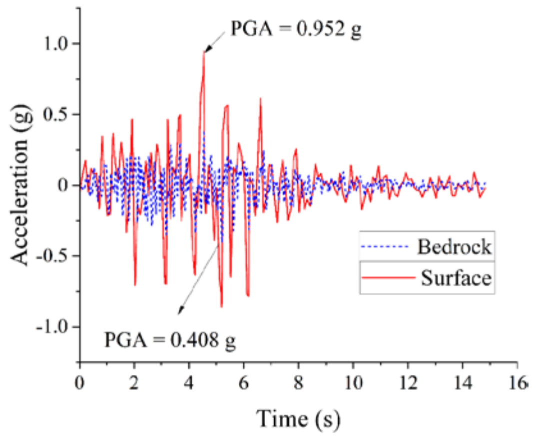

Fig.17 Comparison of ground motion at bedrock and surface levels

These results indicate that the presence of the Ambon Fault can significantly affect ground response at the surface for short periods. This result is consistent with previous research [34], which showed that alluvial soils generally exhibit higher amplification factors than hillside soils do. In addition, the proximity of the site to the fault can significantly affect ground response results. The displacement values at sites near faults tend to be larger than those farther away from faults [35].

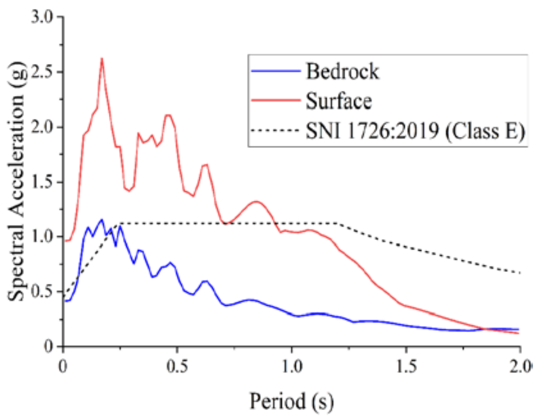

Fig.18 Comparison of response spectrum at bedrock and surface levels

5. CONCLUSION

This study led to several relevant conclusions regarding soil behavior during earthquakes at the site. The use of nonlinear analysis in the 2D finite element method successfully accounted for the increase in the PWP and decrease in the effective stress during the shaking period. This provides a deeper understanding of how PWP and effective stress change in the soil during shaking.

This study also illustrates the liquefaction potential at the site using the features provided by QUAKE/W analysis. In soils with N-SPT values <15 (2.20–5.00 m), there is a potential for liquefaction before the start of the dynamic analysis. In addition, the liquefaction potential increased in all soil layers during the shaking period, suggesting that almost all soils at the site may have experienced liquefaction potential during a strong earthquake.

In addition, the results of this study highlight the amplification phenomenon occurring at the site. At the ground surface, there was a significant increase in PGA, reaching 0.952 g from 0.408 g, with an amplification factor of 2.33. The Ambon Fault, which is adjacent to the site, significantly affected the ground response at the surface for short periods.

The outcomes of this study align with those of prior investigations, demonstrating that alluvial soils exhibit higher amplification factors than hillside soils. These results also provide crucial information on the potential dangers of liquefaction and soil behavior during earthquakes in the Ambon coastal region and may serve as a foundation for the development of infrastructure that is resistant to earthquakes and liquefaction.

6. ACKNOWLEDGMENTS

We express our gratitude to the Ministry of Public Works and Housing of the Republic of Indonesia for their invaluable assistance in providing the data and supporting all aspects of this study.

7. REFERENCES

[1] Lomnitz, C., and Wisner, B. Earthquakes. The Routledge Handbook of Hazards and Disaster Risk Reduction, 2012, pp. 310–321.

[2] Widyatmoko, A., Legono, D., and Hardiyatmo, H. C. Potential Study of Liquefaction in the Downstream Area of Jono Oge-Paneki River, Central Sulawesi. IOP Conference Series: Earth and Environmental Science, Vol. 930, 2021, pp. 1–11.

[3] Bath, M. Earthquake Seismology. Earth-Science Reviews, Vol. 1, No. 1, 1966, pp. 69–86.

[4] Katili, J. A. Tectonic Evolution of Eastern Indonesia and Its Bearing on the Occurrence of Hydrocarbons. Marine and Petroleum Geology, Vol. 8, No. 1, 1991, pp. 70–83.

[5] Sahara, D. P., Nugraha, A. D., Muhari, A., Rusdin, A. A., Rosalia, S., Priyono, A., Zulfakriza, Z., Widiyantoro, S., Puspito, N. T., Rietbrock, A., Lesmana, A., Kusumawati, D., Ardianto, A., Baskara, A. W., Halauwet, Y., Shiddiqi, H. A., Rafie, M. T., Pradisti, R.,

Mozef, P. W., Tuakia, M. Z., and Elly, E. Source Mechanism and Triggered Large Aftershocks of the Mw 6.5 Ambon, Indonesia Earthquake. Tectonophysics, Vol. 799, 2021, pp. 1–13.

[6] Patria, A., Tsutsumi, H., and Natawidjaja, D. H. Active Fault Mapping in the Onshore Northern Banda Arc, Indonesia: Implications for Active Tectonics and Seismic Potential. Journal of Asian Earth Sciences, Vol. 218, 2021, pp. 1–13.

[7] Sengara, I. W., and Sulaiman, A. Nonlinear Dynamic Analysis Adopting Effective Stress Approach of an Embankment Involving Liquefaction Potential. No. 156, S.-J. Hwang, L. Comfort, I. W. Segara, and A. Hakam, eds., 2020, pp. 1–9.

[8] Karlinasari, R., and Rahardjo, P. Case Study and Numerical Modeling for Liquefaction of Soil with Three Possible Phenomenons Cause of Liquefaction, Proceedings of International Conference on "Landslide and Slope Stability" (SLOPE 2019), 2019, pp. 1–9.

[9] Jawad, H. S. H. A., Mashhour, I. M., Akl, S. A. Y., and Abu-keifa, M. A. Effectiveness of Concrete Rigid Inclusions for Coastal Reclaimed Liquefiable Soils. Ain Shams Engineering Journal, Vol. 14, No. 2, 2023, pp. 1–9.

[10] Johari, A., and Heidari, A. Comparison of Equivalent Linear and Nonlinear Ground Response Analysis Methods in the Time Domain, 3rd National & 1st International Conference in applied research on Civil Engineering, Architecture and Urban Planning, 2020, pp. 1–7.

[11] TJokrosapoetro, S., Rusmana, E., and Achdan, A. Geological Map of The Ambon Sheet, Maluku. Center for Geological Survey, Geological Agency, Bandung, Indonesia, 2011.

[12] Kaklamanos, J., Baise, L. G., and Boore, D. M. Estimating Unknown Input Parameters When Implementing the NGA Ground-Motion Prediction Equations in Engineering Practice. Earthquake Spectra, Vol. 27, No. 4, 2011, pp. 1219–1235.

[13] Aglia, G., Wijaya, M., and Rahardjo, P. P. The Study of Seismic Hazard in Near-Fault Areas Using Probabilistic and Deterministic Approach. Journal of the Civil Engineering Forum, Vol. 9 No. 2, 2023, pp. 117–126.

[14] Chiou, B.-J., and Youngs, R. R. An NGA Model for the Average Horizontal Component of Peak Ground Motion and Response Spectra. Earthquake Spectra, Vol. 24, No. 1, 2008, pp. 173–215.

[15] Wells, D., and Coppersmith, K. New Empirical Relationships among Magnitude, Rupture Length, Rupture Width, Rupture Area, and Surface Displacement. Bulletin of the Seismological Society of America, Vol. 84, 1994, pp. 974–1002.

[16] Mai, P., Spudich, P., and Boatwright, J. Hypocenter Locations in Finite-Source Rupture Models. Bulletin of the Seismological Society of America, Vol. 95, 2005, pp. 965–980.

[17] Shahi, S. K., and Baker, J. W. NGA-West2 Models for Ground Motion Directionality. Earthquake Spectra, Vol. 30, No. 3, 2014, pp. 1285–1300.

[18] Mase, L. Z. Performance of NGA Models in Predicting Ground Motion Parameters of The Strong Earthquake. Journal of the Civil Engineering Forum, Vol. 5, No. 3, 2019, pp. 227–236.

[19] Abrahamson, N. A., Silva, W. J., and Kamai, R. Summary of the ASK14 Ground Motion Relation for Active Crustal Regions. Earthquake Spectra, Vol. 30, No. 3, 2014, pp. 1025–1055.

[20] Boore, D. M., Stewart, J. P., Seyhan, E., and Atkinson, G. M. NGA-West2 Equations for Predicting PGA, PGV, and 5% Damped PSA for Shallow Crustal Earthquakes. Earthquake Spectra, Vol. 30, No. 3, 2014, pp. 1057–1085.

[21] Campbell, K., and Bozorgnia, Y. NGA-West2 Ground Motion Model for the Average Horizontal Components of PGA, PGV, and 5% Damped Linear Acceleration Response Spectra. Earthquake Spectra, Vol. 30, 2014, pp. 1087–1115.

[22] Chiou, B. S.-J., and Youngs, R. R. Update of the Chiou and Youngs NGA Model for the Average Horizontal Component of Peak Ground Motion and Response Spectra. Earthquake Spectra, Vol. 30, No. 3, 2014, pp. 1117–1153.

[23] Indonesian Standard Code, Earthquake Resistance Design for Buildings (SNI 03-1726-2019), National Standardization Agency, 2019.

[24] Halldorsson, B. Calibration of the Specific Barrier Model to Earthquakes of Different Tectonic Regions. Bulletin of the Seismological Society of America, Vol. 95, No. 4, 2005, pp. 1276–1300.

[25] Terzaghi, K., and Peck, R. B. Soil Mechanics in Engineering Practice, 2nd Edition. Edited by Karl Terzaghi and R.B. Peck. John Wiley & Sons, 1967, pp. 1–729.

[26] Ameratunga, J., Sivakugan, N., and Das, B. M. Correlations of Soil and Rock Properties

in Geotechnical Engineering. Springer India, 2016, pp. 1–326.
[27] Kumar, R., Bhargava, K., and Choudhury, D. Estimation of Engineering Properties of Soils from Field SPT Using Random Number Generation. INAE Letters, Vol. 1, Nos. 3–4, 2016, pp. 77–84.
[28] Darendeli, M. B., Development of a new Family of Normalized Modulus Reduction and Material Damping Curves, Civil Engineering. Austin: University of Texas at Austin ProQuest Dissertations Publishing, 2001, pp 395.
[29] Anbazhagan, P., Uday, A., Moustafa, S. S. R., and Al-Arifi, N. S. N. Soil Void Ratio Correlation with Shear Wave Velocities and SPT N Values for Indo-Gangetic Basin. Journal of the Geological Society of India, Vol. 89, No. 4, 2017, pp. 398–406.
[30] Martin Geoffrey R., Seed H. Bolton, and Finn W. D. Liam. Fundamentals of Liquefaction under Cyclic Loading. Journal of the Geotechnical Engineering Division, Vol. 101, No. 5, 1975, pp. 423–438.
[31] Sladen, J. A., D'Hollander, R. D., and Krahn, J. The Liquefaction of Sands, a Collapse Surface Approach. Canadian Geotechnical Journal, Vol. 22, 1985, pp. 564–578.
[32] Sladen, J. A., D'Hollander, R. D., Krahn, J., and Mitchell, D. E. Back Analysis of the Nerlerk Berm Liquefaction Slides. Canadian Geotechnical Journal, Vol. 22, No. 4, 1985, pp. 579–588.
[33] Faris Waleed Jawad, Madhat Shakir Al-Soud, Mustafa Musa Salih, N. Al-ansari, and H. Madhloom. Liquefaction Potential of Layered Soil Under Vertical Vibration Loads. GEOMATE Journal, vol. 23, no. 99, Nov. 2022, pp. 141-150.
[34] Tohari, A. Seismic Microzonation of Soil Amplification and Liquefaction for Padang City. E3S Web of Conferences, Vol. 156, 2020, pp. 1–10.
[35] Zhang, S., and Wang, G. Effects of Near-Fault and Far-Fault Ground Motions on Nonlinear Dynamic Response and Seismic Damage of Concrete Gravity Dams. Soil Dynamics and Earthquake Engineering, Vol. 53, 2013, pp. 217–229.